JBO Journal of Biomedical Optics

RESEARCH PAPER

Quadrant darkfield for label-free imaging of intracellular puncta

Tarek E. Moustafa,[a] Rachel L. Belote,[b,c] Edward R. Polanco,[a] Robert L. Judson-Torres,[b,d,e] and Thomas A. Zangle[a,b,*]

[a]University of Utah, Department of Chemical Engineering, Salt Lake City, Utah, United States
[b]University of Utah, Huntsman Cancer Institute, Salt Lake City, Utah, United States
[c]The Ohio State University, Department of Molecular Genetics, Columbus, Ohio, United States
[d]University of Utah, Department of Dermatology, Salt Lake City, Utah, United States
[e]University of Utah, Department of Oncological Sciences, Salt Lake City, Utah, United States

ABSTRACT. **Significance:** Imaging changes in subcellular structure is critical to understanding cell behavior but labeling can be impractical for some specimens and may induce artifacts. Although darkfield microscopy can reveal internal cell structures, it often produces strong signals at cell edges that obscure intracellular details. By optically eliminating the edge signal from darkfield images, we can resolve and quantify changes to cell structure without labeling.

Aim: We introduce a computational darkfield imaging approach named quadrant darkfield (QDF) to separate smaller cellular features from large structures, enabling label-free imaging of cell organelles and structures in living cells.

Approach: Using a programmable LED array as the illumination source, we vary the direction of illumination to encode additional information about the feature size within cells. This is possible due to the varying levels of directional scattering produced by features based on their sizes relative to the wavelength of light used.

Results: QDF successfully resolved small cellular features without interference from larger structures. QDF signal is more consistent during cell shape changes than traditional darkfield. QDF signals correlate with flow cytometry side scatter measurements, effectively differentiating cells by organelle content.

Conclusions: QDF imaging enhances the study of subcellular structures in living cells, offering improved quantification of organelle content compared with darkfield without labels. This method can be simultaneously performed with other techniques such as quantitative phase imaging to generate a multidimensional picture of living cells in real-time.

Keywords: label-free imaging; computational imaging; darkfield microscopy; cellular organelles

Paper 240221GR received Aug. 5, 2024; revised Nov. 10, 2024; accepted Nov. 13, 2024; published Nov. 29, 2024.

1 Introduction

Measuring dynamic reorganization in cellular structure and organelles is vital for the study of disease progression and response to treatment.[1–3] As cells switch phenotypes in response to environmental or genetic signals, corresponding changes are observed in cellular components including mitochondria,[4] endoplasmic reticulum,[5,6] Golgi apparatus,[7] melanosomes,[8,9]

*Address all correspondence to Thomas A. Zangle, tzangle@chemeng.utah.edu

microtubules,[10–12] and the plasma membrane.[13–15] These changes can be related to cellular events such as necrosis,[16] senescence,[17] and the emergence of drug resistance.[8] The quantification of intracellular dynamics, therefore, serves as a critical indicator of a cell's health, behavior, and its response to therapeutic interventions.

Imaging approaches are commonly used to measure changes in subcellular structure. For example, electron microscopy is commonly used to study details of organelle structure in fixed cells[8] but cannot quantify changes in living cells in real time. Fluorescence microscopy has been widely used to study cell structure, including measurement of damage to plasma membranes,[15] measurements of melanosome maturation,[18] localization of nuclei,[19] and tracking lysosomes during autophagy and other cell states.[20,21] However, the need for a fluorescent molecule that binds to the specific target or for a cell to express a fluorescently tagged protein is one of the limiting factors of fluorescence microscopy. In addition, labels can affect cell behavior and the need for high-intensity illumination can cause phototoxicity, especially during live cell imaging.[22]

Intrinsic scattering and autofluorescence can also be used for label-free imaging of cell structures. Side scatter measurements in flow cytometry can be used to quantify changes in subcellular structure without the need for fluorescent labels.[23] Although forward scatter measurements predominantly measure cell size, side scatter reflects the granularity of the internal contents of the cell.[23] However, flow cytometry cannot track changes in the same cell over time.[24] Raman spectroscopy utilizes the weak inelastic scattering of light that is dependent on molecular composition to identify organelles and molecular composition within the cell, such as nucleic acids, mitochondria, and endoplasmic reticulum.[25] However, the Raman signal is typically weak, necessitating the use of high-powered lasers or long exposure times to produce sufficient signal-to-noise ratios.[25] Light scattering spectroscopy (LSS) uses elastic backscattering that is dependent on both wavelength and particle size to measure the concentration and size of organelles.[26–30] For example, the ability of LSS to measure the size of organelles and changes in structure allowed for the detection of precancerous and malignant cells in multiple cancer types.[26,28,29] However, LSS is not an imaging technique and so cannot be used to study the localization of organelles inside cells. Autofluorescence is the natural phenomena of proteins emitting light when excited using a suitable wavelength without the use of labels.[31] However, the main limitations of autofluorescence are the low signal that organelles produce, the need for a specific wavelength of light for each organelle, and the limited number of organelles and structures that are naturally fluorescent without labeling.[31]

Computational microscopy provides methods to measure the intrinsic contrast caused by refractive index variation within cells. Multiple organelles, including lysosomes and mitochondria, differ slightly in density and refractive index from the surrounding cytoplasm.[32,33] This difference can be quantified using quantitative phase imaging (QPI)[34] which measures phase shift as light passes through the cell.[35,36] One recent example used QPI to track lysosomes in living cells without the use of fluorescent tags.[32] Although the current trends and advances including using AI to identify organelles are promising,[37] tracking organelles can be difficult with two-dimensional QPI due to the signal from overlapping cell components. Three-dimensional computational methods such as Fourier ptychography,[38] holography,[39] or three-dimensional differential phase contrast[40] provide the needed information to resolve density or refractive index changes in each 3D voxel within the cells. However, these techniques require either tens of images per field of view, limiting their temporal resolution and their ability to conduct high throughput experiments in multi-well plates or the use of relatively more complex optical systems, hindering integration with other techniques to provide multidimensional orthogonal data about the biological sample.

Some of the simplest techniques to study changes in cellular structure are brightfield and darkfield imaging. Brightfield signal correlates with absorption which is usable in studying organelles such as melanosomes that absorb light,[41] but limited for other cell structures. On the other hand, many subcellular features scatter light due to variations in refractive index between organelles and cytoplasm.[42] For cellular organelles (0.1 to 10 μm) imaged using visible light (380 to 700 nm), this scattering is explained using Mie scattering theory[23,43] and features within this size range can be detected using darkfield imaging. Early uses of darkfield were to detect contaminants in blood samples and to differentiate cell types due to its inherent contrast even between objects close to the refractive index of the media used.[44] Since then, darkfield has been

used to quantitatively measure the size of red blood cells,[45] to track in real-time respiratory syncytial virus infecting cells using gold nanoparticles,[46] to measure nanoparticle distribution in lung cells,[47] and to visualize and count sub-micron particles in suspension.[48] When performing darkfield using transillumination, larger features, such as the boundaries of cells, tend to have higher signals. This is due to more directional refraction of light into the objective from large features.[43,49,50] As the feature size gets smaller, the light starts to scatter in a cone, bending more light away from the objective and decreasing the signal. For a given wavelength, this cone keeps growing as the feature size gets smaller leaving only a negligible amount of light to be collected by the objective. This change is commonly used for sizing particles.[49–51] In addition, the difference in directionality between larger and smaller objects means that illumination from different directions can potentially resolve different features based on size.

In this paper, we develop a computational darkfield approach we call quadrant darkfield (QDF). QDF differentially resolves smaller cellular features which scatter broadly as explained by Mie scattering ($\sim\lambda$) from larger features that more uniformly refract light ($\gg\lambda$). This allows imaging of small features of the cell such as cellular structures and organelles without interference from larger structures such as cell edges. We demonstrate QDF on an inverted microscope using a programmable LED array as the light source. This approach can be used simultaneously with other modalities such as QPI to collect multimodal images of cells in standard multi-well plates. Here, we demonstrate QDF's ability to resolve features in polystyrene beads and both pigmented melanoma cells and non-pigmented breast cancer cells. We demonstrate that QDF is not impacted by changes in shape such as those that occur during cell division, in contrast to traditional darkfield which is highly dependent on cell shape. Finally, we show concordance between the QDF signal and side scatter from flow cytometry to differentiate melanoma cells with different levels of pigmentation.

2 Materials and Methods

2.1 Darkfield and QDF Data Acquisition

QDF was performed on a custom-built microscope consisting of a 0.25 NA, 10× objective (PLN 10×, Olympus, Japan), a monochrome 1920 × 1200 CMOS camera (GS3-U3-23S6M-C, Teledyne FLIR, United States), and a 180 mm tube lens [Fig. 1(a)].[52] The LED array was illuminated between 1.05× to 1.33× $\mathrm{NA}_{\mathrm{objective}}$ [Fig. 1(b)]. Four images were captured using quadrant darkfield illumination patterns [Fig. 1(c)] at an exposure time of 220 ms and a gain of 25 dB. Darkfield images were computed by summing the four quadrant images. For QDF processing, the quadrant images were combined to compute the edge image, E, as

$$E = |\mathrm{TL} - \mathrm{BR}| + |\mathrm{BL} - \mathrm{TR}|, \tag{1}$$

where TL, BR, BL, and TR refer to images captured under top-left, bottom-right, bottom-left, and top-right illumination, respectively [Fig. 1(b)]. All operations are performed pixel-wise. The edge image was then subtracted from a scaled darkfield image to produce the QDF image

$$\mathrm{QDF} = c \times \mathrm{DF} - E, \tag{2}$$

where c is a scaling factor that is system-specific and determined experimentally to match the darkfield signal at the edge of objects with the edge image and is typically in the range of 0.8 to 1.0 depending on the experimental setup (See discussion in the Supplementary Material).

2.2 QPI Data Acquisition

QPI was obtained using differential phase contrast (DPC) and reconstructed using Tikhonov deconvolution.[53,54] DPC images were captured with an exposure time of 50 ms, a gain of 25 dB, a coherence parameter of 1.25, and a regularization parameter of 4×10^{-3}, which was determined experimentally as described previously.[52]

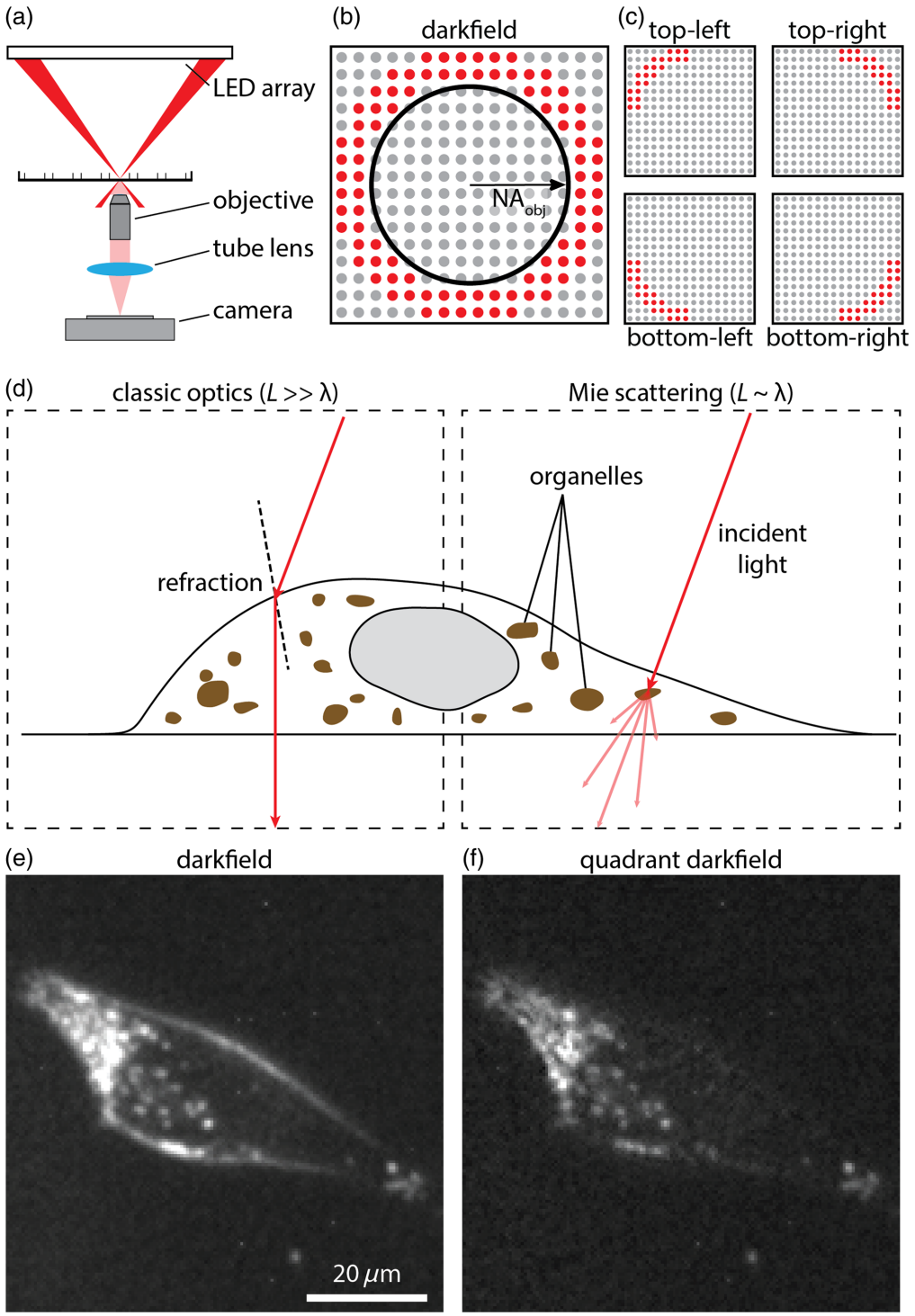

Fig. 1 (a) Schematic diagram of an inverted microscope with an LED array as a light source in a darkfield illumination setup. (b) Bottom-up view of the LED array illumination pattern in a darkfield with the numerical aperture of the objective superimposed. (c) The illumination pattern used for each of the quadrants in QDF. (d) Diagram showing how light is directionally refracted by large features according to Snell's law (left) relative to how light is scattered when hitting a subcellular feature according to Mie scattering theory (right). (e) Darkfield image of a melanoma PDX cell (MTG021). (f) QDF image of the same cell from panel (e).

2.3 Cell Culture

2.3.1 *MDA-MB-231*

MDA-MB-231 were acquired from ATCC (HTB-26, ATCC, United States) and passaged on 100 mm plates (12-567-650, Thermo Fisher Scientific, United States) in RPMI (11875093, Thermo Fisher Scientific) with 10% FBS (10-437-028, Thermo Fisher Scientific) and 1% Penicillin-Streptomycin (15-140-122, Thermo Fisher Scientific). For passaging, cells were washed with Dulbecco's phosphate-buffered saline (14-190-144, Thermo Fisher Scientific) and then incubated with Trypsin (15-400-054, Thermo Fisher Scientific) at 37°C and 5% CO_2 for 7 min followed by trypsin deactivation using RPMI medium at 1:1 ratio. The dissociated cell suspension was centrifuged at $400 \times g$ at room temperature for 4 min before resuspension in RPMI medium and splitting at a 1:4 ratio.

2.3.2 *MTG084 and MTG021*

MTG084 (AM084) and MTG021 (ASM021) cells were previously generated from patient-derived xenograft (PDX) models of melanoma (Huntsman Cancer Institute, Preclinical Research Resource)[55] and grown in AM3 media (80% MCDB153 (#M7403, Sigma, United States), 20% L-15 media (#11415-064, Thermo Fisher Scientific), 2.5% FBS (#FB5001-H, Thermo Fisher Scientific), 1X Insulin-Transferrin-Selenium X (#51500-056, Thermo Fisher Scientific), 5 ng/mL EGF, 0.2% BPE, 10 ng/mL insulin-like growth factor, 5 μg/mL transferrin, 3 ng/mL BFGF, 3 μg/mL heparin, 0.18 μg/mL hydrocortisone, 10 nM endothelin 1, and 1.68 mM CaCl2) in 5% CO_2 at 37°C.

2.4 Image Acquisition and Processing

2.4.1 *Image acquisition*

Cells were plated at 12,500 cells in each well of a 24-well plate (7000674, Greiner Bio-One, Germany) for imaging. Cells were incubated for 24 h (MDA-MB-231) or 48 h (MTG021 and MTG084) prior to imaging and placed inside the microscope incubator for 30 to 45 min prior to imaging. Cells were imaged every 20 min with a single autofocus between imaging cycles to account for thermal and z-stage drift. Nine imaging positions were chosen at the center of each well to avoid scattering from the edges of the well.

2.4.2 *QPI processing*

QPI images were background corrected by masking cells and fitting an eighth-order polynomial to background pixels that were subtracted from the raw phase image. Single cells were segmented using a watershed algorithm, and cell dry mass was computed using a cell average-specific refractive increment of 1.8×10^{-4} m^3/kg.[35] Segmented cells were tracked over time using the Crocker-Grier algorithm[56] to aid in the detection of debris.

2.4.3 *Darkfield image processing*

Darkfield images were scaled down to 12 bits by dividing by 16 and rounding to the nearest integer to match the camera bit depth. An image from an empty reference position was subtracted from darkfield images to remove the background signal. An eighth-order polynomial fit was removed from the background of masked quadrant and edge images.

2.5 Flow Cytometry

Cells were harvested using 0.05% trypsin (#25300054, Thermo Fisher Scientific) followed by trypsin deactivation with 1:1 Soybean Trypsin Inhibitor (#17075029, Thermo Fisher Scientific). The dissociated cell suspension was centrifuged at 500 g, 4°C, for 4 min, and resuspended in ice-cold FACS buffer (0.1% BSA, 2.5% HEPES, in HBSS). Single-cell suspensions were counted, diluted to 1×10^6 cells per 300 to 500 μl in ice-cold FACS buffer, and passed through a 35 μm filter. Flow cytometry was performed using a BD FACS Aria sorter (BD, United States),

BD Fortessa analyzer (BD, United States), and SONY SH800 sorter (SONY, Japan). SSC (Aria and Fortessa)/BSC (SONY) analysis was conducted on single cells by gating to exclude debris and doublets using a two-step doublet discrimination gating strategy first with FSC-A vs FSC-H followed by SSC-A vs SSC-H or BSC-A vs BSC-H.

2.6 Statistics

Segmented objects were filtered using thresholds of area, track length, and averages of phase shift, darkfield, and QDF to remove debris. Segmented cells were manually inspected to remove the under-segmentation of multiple cells and the over-segmentation of single cells. A least-squares linear regression was applied to QDF and darkfield signals against mass per area. Linear fits were evaluated relative to the null hypothesis of a better fit to a flat line parallel to the y-axis using an F-test with a p value of 0.05. Correlation between variables was computed using the Pearson correlation coefficient in Matlab (Matlabs R2021a, Mathworks, United States). Kullback-Leibler divergence was computed using the relativeEntropy function in Matlab (Matlabs R2021a, Mathworks, United States). A two-sample t-test was computed using ttest2 function in Matlab (Matlabs R2021a, Mathworks, United States).

2.7 Signal-to-Noise Ratio Calculation

To quantify the signal, a threshold mask equal to 4× the 99th percentile of the background signal in each image was applied to each QDF image. The intersection of single-cell labels and the threshold mask is the QDF signal from puncta in each cell. The noise level is defined as the standard deviation of the background signal outside masked cells. Results are reported as mean $\pm$ standard deviation.

2.8 Bead Sample Preparation

20 μm diameter polystyrene beads (18329-5, Polysciences, United States) were embedded in NOA73 (NOA73, Norland Products, United States) sandwiched between a standard microscope slide (12-544-4, Fisher scientific, United States) and a no. 1.5 cover glass (22-037-082, Fisher scientific) and cured under ultraviolet radiation (IntelliRay, Uvitron, United States).

2.9 Digital Edge Detection

Each image was filtered using a Gaussian filter with a standard deviation of two pixels. A Sobel or Canny filter was applied with varying thresholds. A dilation structure was used to expand the binary mask with varying sizes.

3 Results

The use of an LED array as an illumination source [Fig. 1(a)] enables the display of different illumination schemes, such as a ring of LEDs outside the numerical aperture of the objective lens for darkfield imaging [Fig. 1(b)].[53] In QDF, this darkfield illumination ring is divided into four quadrants [Fig. 1(c)]. This setting allows each image acquired under a unique quadrant ring illumination pattern to capture angle-specific interactions with the sample. In living cells, there are two main types of scattering based on the relative size of the cellular feature to the wavelength of light used for imaging. Features much larger than the wavelength, e.g., the outer cell membrane act as lenses that primarily refract light. Thus, the path of light can be predicted by classical optics [Snell's Law, Fig. 1(d)]. For features close in size to the wavelength, e.g., sub-cellular puncta or organelles, the path of light can be explained by Mie scattering theory [Fig. 1(d)]. Features of both sizes generate a sufficient signal to be captured in the darkfield [Fig. 1(e)]. However, the larger features (e.g., cell boundaries) often obscure the smaller features (e.g., organelles), especially near cell edges. QDF separates the darkfield signal based on the directionality of light allowing for a cleaner image of sub-cellular features [Fig. 1(f)].

To validate feature differentiation with QDF, we embedded 20 μm polystyrene beads into an optical adhesive for use as an imaging phantom. When imaged in darkfield, these beads behave as spherical lenses with the center rays passing straight through and the edges refracting light, resulting in the bead edges appearing as a bright ring [Fig. 2(a)]. In most beads, some weaker signals inside and outside the bead due to diffraction around the bead as well as light from other

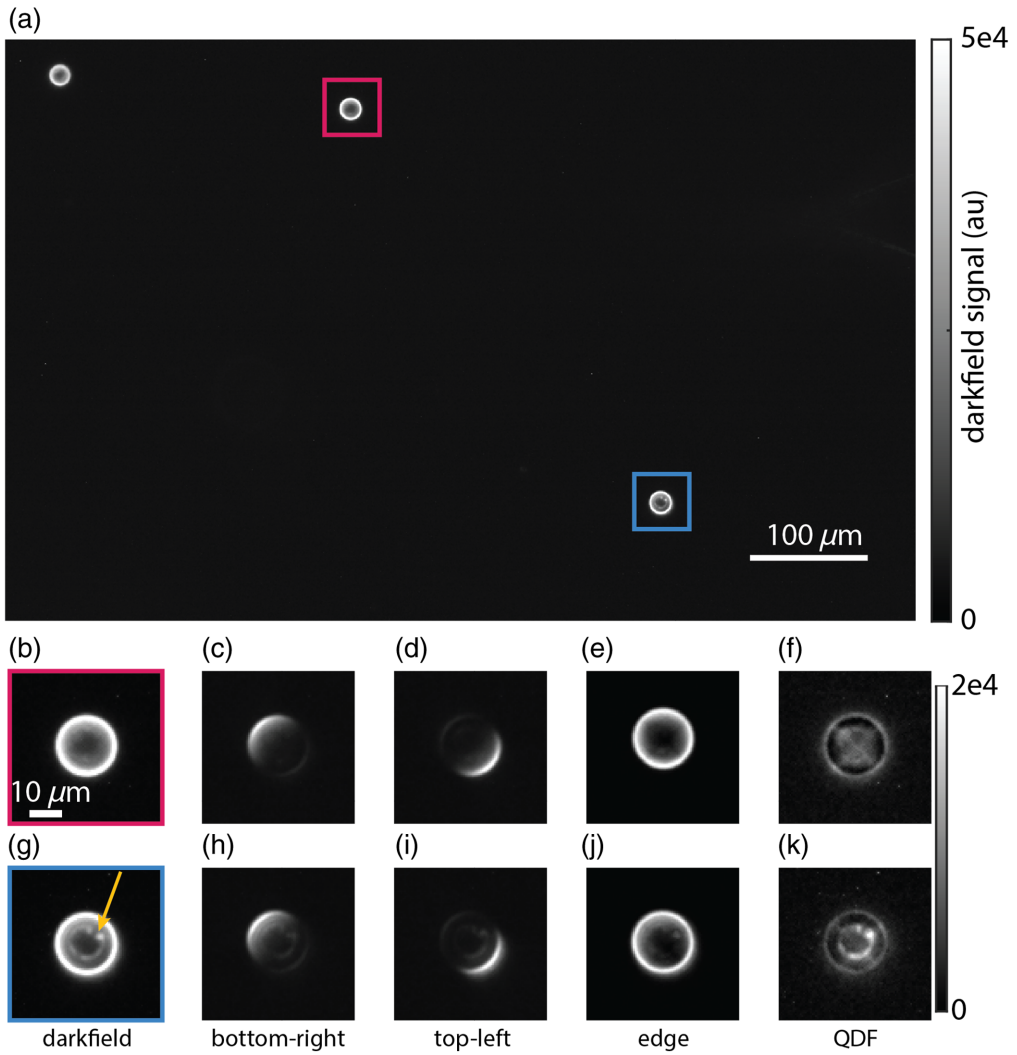

Fig. 2 (a) Full field of view image of 20 μm polystyrene beads in darkfield. (b) Zoomed in darkfield image of a clean bead. (c) Top-left illuminated quadrant image of the clean bead. (d) Bottom-right illuminated quadrant image of the clean bead. (e) The resulting edge image from combining the four quadrants. (f) QDF image of the clean bead. (g) Zoomed-in image of the imperfect bead. The arrow highlights visible imperfections. (h) Top-left illuminated quadrant image of the imperfect bead. (i) Bottom-right illuminated quadrant image of the imperfect bead. (j) The resulting edge image from combining the four quadrants. (k) QDF image of the imperfect bead. Red and blue boxes in panel (a) correspond to fields of view in panels (b)–(f) and (g)–(k), respectively.

out-of-focus sections of the bead are also observed [Fig. 2(b)]. Under asymmetric quadrant illumination, we observe light being refracted by the opposing quarter of the bead [Figs. 2(c)–2(d)]. When we combine the quadrants into an edge image [Eq. (1)], the edges of the bead are captured clearly [Fig. 2(e)]. Subtraction of this edge image in QDF removes nearly all the signal from most beads [Fig. 2(f)]. Some residual signal remains, possibly due to diffraction from the edge of the object opposite to the edge that is visible due to scattered light. This is accounted for by the scaling factor, c, in the QDF image calculation [Eq. (2) and Supplementary Material]. We also observed a number of beads with imperfections, possibly due to material deformations or the accumulation of impurities as the beads dry on top of the glass slide.[57] Looking closer at an imperfect bead [Fig. 2(g)], darkfield imaging shows both the imperfection as well as the bead edge. Under asymmetric quadrant illumination, the imperfection is always present in all images along with the opposing edge [Figs. 2(h), 2(i)]. This validates that the signal from the smaller features is less directionally dependent on the angle of illumination in the darkfield when compared with the signal from the edges. Thus, when the quadrant images are combined [Eq. (1)],

the resulting edge image primarily has a signal from the edges. When the QDF image is computed, the imperfections at the center of the bead are observed clearly without being obscured by signal from the edges [Fig. 2(k)]. QDF is fundamentally based on optical edge detection and removal; therefore, we also compared QDF with digital edge detection methods with Canny and Sobel filters. We find that compared with digital edge detection methods, QDF more consistently detects edges of polystyrene beads and reveals structures such as imperfections within them (Fig. S1 in the Supplementary Material).

Next, we applied QDF to a melanoma cell line, as they have an abundance of melanosomes, pigment-producing lysosome-related organelles, with a size range between ~100 nm and 1 μm.[9,58] Within this size range, Mie theory predicts that QDF will be able to separate subcellular features from cell edges due to the broad directionality of scattering from organelles relative to the directional uniform scattering at cell boundaries. We additionally imaged the cells using QPI to aid in segmenting the cells [Fig. 3(a)]. In darkfield, cells show varied signals based on shape and cellular content with more rounded cells producing higher signals from the edges [Fig. 3(b)]. Using QDF, we were able to differentiate smaller features within cells from cell edges giving a clear view of puncta inside the cells. QPI also quantifies the dry mass of cells and helps differentiate flat from more rounded cells based on the density at each pixel[59] [Fig. 3(d)]. When we view two cells with high mass density (reflecting cell rounding) and low mass density (reflecting a flatter cell morphology) in darkfield, the difference in signal from cell edges is apparent [Fig. 3(e)]. In these same cells, the edge image [Eq. (1)] shows the edge of each cell [Fig. 3(f)]. The resulting QDF image shows a much greater contrast in intracellular puncta [Fig. 3(g)]. In addition, we characterized the signal-to-noise ratio (SNR) of individual puncta resolved by QDF in MTG021 as 31 ± 6 (Fig. S2 in the Supplementary Material). In MTG084, an additional melanoma cell line with different pigmentation, the QDF SNR was 24 ± 5.

One of the issues with using traditional darkfield imaging for longitudinal tracking of subcellular features is the dependency of the signal from cell edges on the shape of the cell. Cell morphology changes naturally throughout the cell cycle. For example, adherent cells become rounded just prior to cell division.[60,61] To validate QDF signal independence from shape, we imaged a breast cancer cell line that does not contain melanosomes [Fig. 4(a)].

As an example of the shape changes that occur during cell cycle progression, we followed one individual cell as it changes shape from flat to rounded over 40 min [Fig. 4(b)]. In darkfield, the signal increases significantly due to the additional lensing effect of the rounded edges of the cell [Fig. 4(c)]. By looking at the computed edge images [Eq. (1)], the difference in the brightness

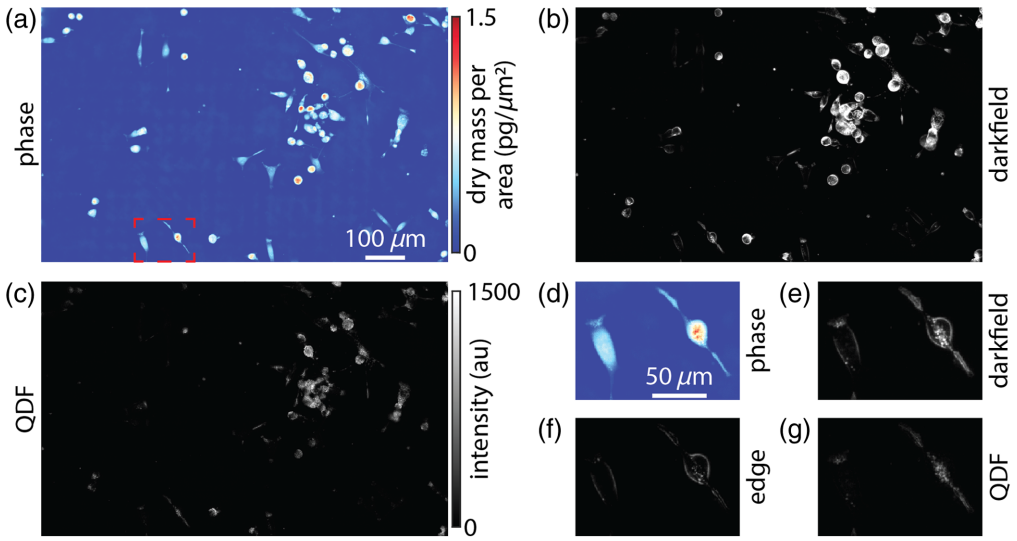

Fig. 3 Melanoma cell line MTG021 imaged via (a) QPI, (b) darkfield, and (c) QDF. (d) QPI of two adjacent cells of varying shape and mass density from the outlined region in panel (a). (e) Darkfield image of these cells. (f) Edge image resulting from the quadrant image processing. (g) Resulting QDF image of the two cells.

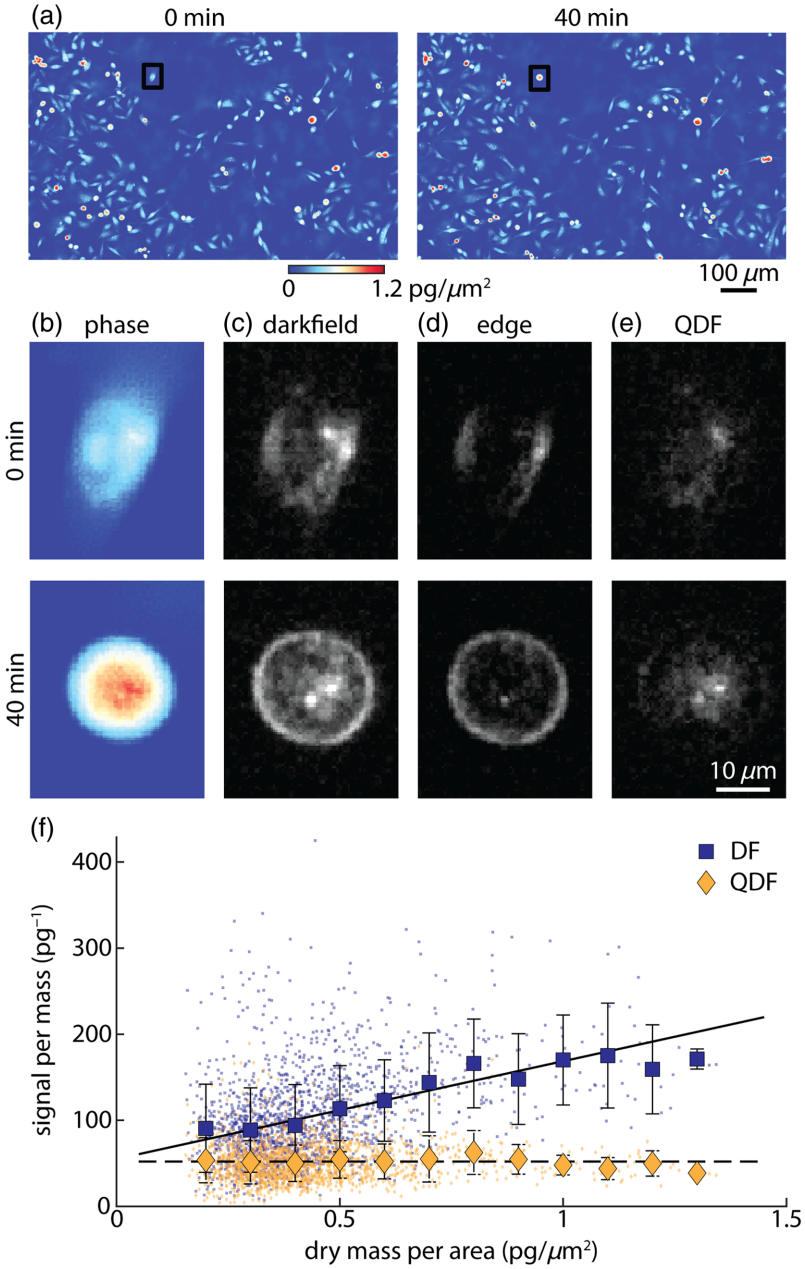

Fig. 4 (a) Phase images of MDA-MB-231 breast cancer cells, (b) darkfield images, (c) edge images, and (d) QDF images. Sub-images in panels (b)–(e) correspond to black-boxed cells in panel (a). (e) Scatter plot of darkfield (dark blue) and QDF (dark yellow) per mass (y-axis) against mass per area (x-axis) as a proxy of shape change. Larger points are the average within bins of 0.1 pg/μm^2. Error bars show the standard deviation within each bin. Lines show linear fits to the data as an indication of the overall trend (solid: darkfield, DF; dashed: QDF).

of the edges is drastic [Fig. 4(d)]. In the resulting QDF images, the density of the signal increases more moderately as the puncta are pulled closer to each other [Fig. 4(e)]. During this transition, the total darkfield signal increased by 40%. On the other hand, the total QDF signal change was 5%. This is within the accuracy limits of our system, reflecting that the total organelle content of the cell did not appreciably change over this period. When analyzing the QDF and darkfield signal on a population basis, the dependency of darkfield on shape, as measured using mass per area,[59] is clear (Fig. S3 in the Supplementary Material). QDF does show a weak dependency on the mass per area, potentially due to an increase in mass resulting in an increase in scattering organelle content. This is confirmed by looking at darkfield and QDF signal per mass against

mass per area [Fig. 4(f)]. When fitted with a linear fit, these data indicate that the darkfield signal is significantly more dependent on cell shape than QDF (Pearson's correlation coefficient, R, for darkfield = 0.39 and for QDF = 0.02; Goodness of fit, R^2, for darkfield = 0.15 and for QDF $= 6.1 \times 10^{-4}$). When plotting QDF against mass (Fig. S4 in the Supplementary Material), QDF shows a strong dependency on mass ($R_{\mathrm{QDF}} = 0.60$). However, this dependency is not perfectly linear. As with polystyrene beads, we applied digital edge detection based on Sobel and Canny filters to cells. Again, we find that digital edge detection failed to successfully separate edges and puncta (Fig. S5 in the Supplementary Material), with generally worse performance than observed in polystyrene beads (Fig. S1 in the Supplementary Material). This is possibly due to the closer match in darkfield signal intensity between edges and intracellular features than observed between bead edges and smaller features within beads. A close match in edge and intracellular signals makes it more difficult to choose filter parameters that accurately segment cell edges and do not also obscure intracellular features. This highlights the utility of QDF, which detects edges based on optical properties of cell boundaries.

Finally, we examined the use of QDF to differentiate pigmentation in melanoma cell lines with varying levels of pigmentation [Fig. 5(a)]. Flow cytometry was able to differentiate the two cell lines based on side scatter [Figs. 5(b), S6 in the Supplementary Material]. In QDF images of the two cell lines, the difference in puncta can clearly be seen [Fig. 5(c)]. Total QDF was also able to differentiate the two different cell lines [Fig. 5(d)], similar to flow cytometry. On the other hand, darkfield shows significantly more overlap between the two cell lines when compared to QDF (Fig. S7 in the Supplementary Material) and cannot localize puncta as clearly as QDF [Fig. 1(e), 1(f), and Fig. S8 in the Supplementary Material]. We performed a two-sample t-test to compare means of the two populations of cells and found a p-value of 2×10^{-113} for QDF and a p-value of 0.71 for darkfield. In addition, to estimate the differences between the distributions of QDF and darkfield signal, we computed relative entropy based on Kullback-Leibler divergence, D_{KL}, which measures the difference between two probability density functions. A larger D_{KL} indicates a larger difference in the distributions. We found that D_{KL}, for QDF $= 8.4 \times 10^{-2}$

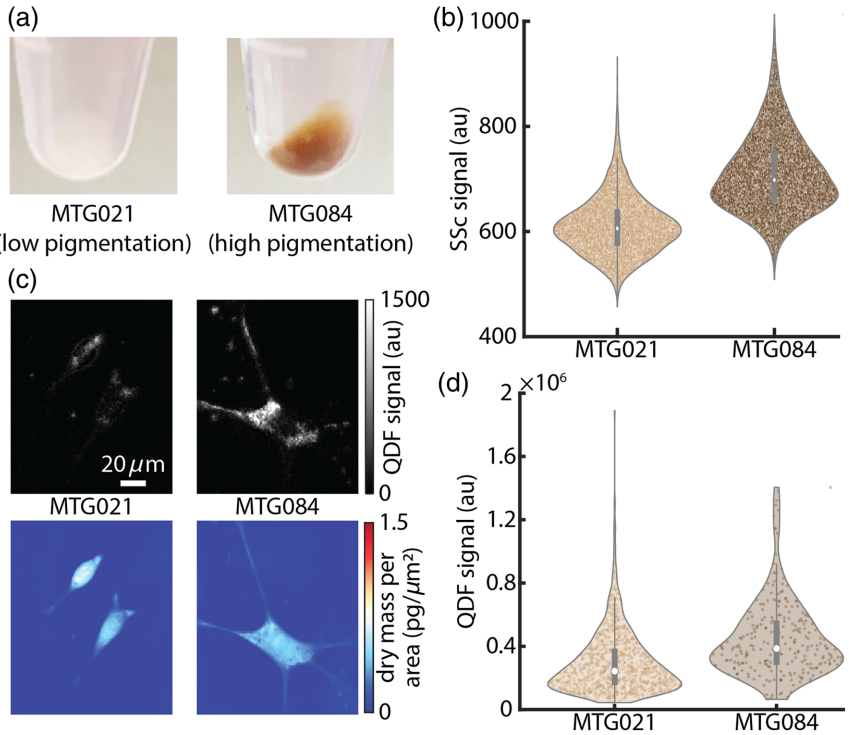

Fig. 5 (a) Cell pellets of two melanoma cell lines with significant differences in pigmentation. (b) Distributions of side scatter measurements from flow cytometry for the two cell lines. (c) QDF and QPI images of example cells for each cell line. (d) Distributions of QDF measurements of the two cell lines.

and D_{KL} for darkfield $= 0.41 \times 10^{-2}$ indicating the increased separation between distributions from MTG084 and MTG021 when using QDF as compared with darkfield.

4 Discussion and Conclusion

Here, we demonstrated QDF as a label-free technique for imaging sub-cellular puncta. Unlike darkfield, QDF signal does not depend on cell shape providing a more reliable quantitative measurement of sub-cellular structure. We also find that QDF is superior to digital edge detection, especially when applied to cells. In addition, the edge measurement used to compute QDF images can be used as a fast indicator for shape change to signal stress or cell cycle events such as division. This can potentially aid in better cell lineage tracking over time. We also demonstrated that QDF can be used to measure pigment-containing melanosomes within melanoma cell lines, with correlation to flow cytometry.

It should also be noted that QDF shares some limitations with darkfield. These limitations include the need for alignment to avoid stray light, the use of a bright illumination source for increased SNR, and the imaging of thin samples to avoid scattering from out-of-focus layers. QDF is diffraction-limited, just as for conventional darkfield or brightfield imaging. Based on Mie theory, the minimum size of observable particles with QDF is approximately one-fifth of the wavelength of light used due to a sharp drop in scattering signal beyond this point.[43,62] Here, we demonstrated QDF's ability to separate large and small cellular features based on their interaction with light and showed a correlation with flow cytometry in the measurement of organelle content. However, as with many other label-free methods such as QPI or phase contrast, QDF lacks the specificity required to differentiate different kinds of puncta and organelles. Therefore, future work should incorporate additional modalities that are capable of labeling specific organelles, such as fluorescence, to more conclusively identify the source of the QDF signal.

As a computational imaging technique, QDF is relatively low to moderate in complexity. In contrast to 3D ptychographic methods which require hundreds of images to be captured,[40,63,64] QDF differentiates subcellular structures using four images. This enables the use of QDF for applications requiring high throughput, such as drug screening applications.[65]

We showed that QDF was able to distinguish puncta inside cells of different masses (Fig. 3) and from different origins including a breast cancer cell line and a non-pigmented melanoma line [Figs. 4(c), 5(c)]. The ability of QDF to monitor subcellular heterogeneity within a single population [Figs. 4(f), 5(d)] is of great potential as an indicator of emerging resistance in melanoma.[8] QDF signal in more mature cells showed brighter puncta which can potentially be used to track melanosome maturation.[9] In addition, QDF can be performed simultaneously with QPI to increase the dimensionality of the data which can improve phenotype-based drug response assays.[65]

Compared with flow cytometry, QDF is inherently an imaging technique that produces detailed images of cells. These images can be used to study subcellular dynamics over time.[66] QDF can be integrated with other modalities, including fluorescence imaging, for better characterization of cellular puncta.

Disclosures

The authors declare no conflict of interest regarding this work.

Code and Data Availability

Data and code are publicly available to recreate the findings of this paper. Associated data is available at doi: https://doi.org/10.5281/zenodo.13227201. The code is available at github.com/Zangle-Lab/QDF.

Acknowledgments

This paper was supported by grants from the National Cancer Institute of the National Institutes of Health (Grant No. 1R01CA276653, TAZ, and RLJT), DoD CDMRP (Grant No. W81XWH2210495, RLB), and the University of Utah (1U4U Grant, TAZ, and RLJT). We utilized the Huntsman Cancer Institute Shared Resource for Preclinical Research Resource and funding from the Cell Response

and Regulation Program (TAZ and RLJT), both supported by the National Cancer Institute of the National Institutes of Health (Award No. P30CA042014).

References

1. S. M. Shaffer et al., "Rare cell variability and drug-induced reprogramming as a mode of cancer drug resistance," *Nature* **546**(7658), 431–435 (2017).
2. E. Danielson and S. H. Lee, "SynPAnal: software for rapid quantification of the density and intensity of protein puncta from fluorescence microscopy images of neurons," *PLoS One* **9**(12), e115298 (2014).
3. E. van der Pol et al., "Single vs. swarm detection of microparticles and exosomes by flow cytometry," *J. Thromb. Haemost.* **10**(5), 919–930 (2012).
4. E. Bahar et al., "Chemotherapy resistance: role of mitochondrial and autophagic components," *Cancers* **14**(6), 1462 (2022).
5. S. Moon et al., "Spectrally resolved, functional super-resolution microscopy reveals nanoscale compositional heterogeneity in live-cell membranes," *J. Am. Chem. Soc.* **139**(32), 10944–10947 (2017).
6. D. S. Schwarz and M. D. Blower, "The endoplasmic reticulum: structure, function and response to cellular signaling," *Cell Mol. Life Sci.* **73**(1), 79–94 (2016).
7. R. Bajaj et al., "Dance of the Golgi: understanding Golgi dynamics in cancer metastasis," *Cells* **11**(9), 1484 (2022).
8. K. G. Chen et al., "Influence of melanosome dynamics on melanoma drug sensitivity," *J. Natl. Cancer Inst.* **101**(18), 1259–1271 (2009).
9. M. d'Ischia et al., "Melanins and melanogenesis: from pigment cells to human health and technological applications," *Pigment Cell Melanoma Res.* **28**(5), 520–544 (2015).
10. I. B. Alieva et al., "The leading role of microtubules in endothelial barrier dysfunction: disassembly of peripheral microtubules leaves behind the cytoskeletal reorganization," *J. Cell Biochem.* **114**(10), 2258–2272 (2013).
11. D. B. Jaunky et al., "Characterization of a recently synthesized microtubule-targeting compound that disrupts mitotic spindle poles in human cells," *Sci. Rep.* **11**(1), 23665 (2021).
12. A. Weber et al., "Microtubule disruption changes endothelial cell mechanics and adhesion," *Sci. Rep.* **9**(1), 14903 (2019).
13. C. Dias and J. Nylandsted, "Plasma membrane integrity in health and disease: significance and therapeutic potential," *Cell Discov.* **7**(1), 4 (2021).
14. R. Itri et al., "Membrane changes under oxidative stress: the impact of oxidized lipids," *Biophys. Rev.* **6**(1), 47–61 (2014).
15. K. Nakajima et al., "Changes in plasma membrane damage inducing cell death after treatment with near-infrared photoimmunotherapy," *Cancer Sci.* **109**(9), 2889–2896 (2018).
16. C. Divei et al., "Analysis and discrimination of necrosis and apoptosis (programmed cell death) by multi-parameter flow cytometry," *Biochim. Biophys. Acta (BBA) - Mol. Cell Res.* **1133**(3), 275–285 (1992).
17. S. W. Sherwood et al., "Defining cellular senescence in IMR-90 cells: a flow cytometric analysis," *Proc. Natl. Acad. Sci. U. S. A.* **85**(23), 9086–9090 (1988).
18. S. Benito-Martínez et al., "Research techniques made simple: cell biology methods for the analysis of pigmentation," *J. Invest Dermatol.* **140**(2), 257–268.e8 (2020).
19. B. I. Tarnowski, F. G. Spinale, and J. H. Nicholson, "DAPI as a useful stain for nuclear quantitation," *Biotech. Histochem.* **66**(6), 296–302 (1991).
20. T. Haller et al., "The lysosomal compartment as intracellular calcium store in MDCK cells: a possible involvement in InsP3-mediated Ca2+ release," *Cell Calc.* **19**(2), 157–165 (1996).
21. Y. S. Rajawat, Z. Hilioti, and I. Bossis, "Aging: central role for autophagy and the lysosomal degradative system," *Ageing Res. Rev.* **8**(3), 199–213 (2009).
22. A. Ettinger and T. Wittmann, "Fluorescence live cell imaging," *Methods Cell Biol.* **123**, 77–94 (2014).
23. K. M. McKinnon, "Flow cytometry: an overview," *Curr. Protoc. Immunol.* **120**, 5.1.1–5.1.11 (2018).
24. K. Minoura et al., "Model-based cell clustering and population tracking for time-series flow cytometry data," *BMC Bioinf.* **20**(Suppl. 23), 633 (2019).
25. S. Siddhanta et al., "Advances in Raman spectroscopy and imaging for biomedical research," *Adv. Opt. Photonics* **15**(2), 318–384 (2023).
26. V. Backman et al., "Polarized light scattering spectroscopy for quantitative measurement of epithelial cellular structures in situ," *IEEE J. Sel. Top. Quantum Electron.* **5**(4), 1019–1026 (1999).
27. I. Itzkan et al., "Confocal light absorption and scattering spectroscopic microscopy monitors organelles in live cells with no exogenous labels," *Proc. Natl. Acad. Sci. U. S. A.* **104**(44), 17255–17260 (2007).
28. L. Zhang et al., "Light scattering spectroscopy identifies the malignant potential of pancreatic cysts during endoscopy," *Nat. Biomed. Eng.* **1**, 0040 (2017).
29. L. T. Perelman et al., "Observation of periodic fine structure in reflectance from biological tissue: a new technique for measuring nuclear size distribution," *Phys. Rev. Lett.* **80**(3), 627–630 (1998).

30. J. R. Mourant et al., "Predictions and measurements of scattering and absorption over broadwavelength ranges in tissue phantoms," *Appl. Opt.* **36**(4), 949–957 (1997).
31. A. C. Croce and G. Bottiroli, "Autofluorescence spectroscopy and imaging: a tool for biomedical research and diagnosis," *Eur. J. Histochem.* **58**(4), 2461 (2014).
32. G. Giugliano et al., "Investigation on lysosomal accumulation by a quantitative analysis of 2D phase-maps in digital holography microscopy," *Cytometry Part A* **105**(5), 323–331 (2024).
33. R. M. Pasternack, J. Y. Zheng, and N. N. Boustany, "Optical scatter changes at the onset of apoptosis are spatially associated with mitochondria," *J. Biomed. Opt.* **15**(4), 040504 (2010).
34. T. L. Nguyen et al., "Quantitative phase imaging: recent advances and expanding potential in biomedicine," *ACS Nano* **16**(8), 11516–11544 (2022).
35. T. A. Zangle and M. A. Teitell, "Live-cell mass profiling: an emerging approach in quantitative biophysics," *Nat. Methods* **11**(12), 1221–1228 (2014).
36. Y. Park, C. Depeursinge, and G. Popescu, "Quantitative phase imaging in biomedicine," *Nat. Photonics* **12**(10), 578–589 (2018).
37. J. Park et al., "Artificial intelligence-enabled quantitative phase imaging methods for life sciences," *Nat. Methods* **20**(11), 1645–1660 (2023).
38. G. Zheng et al., "Concept, implementations and applications of Fourier ptychography," *Nat. Rev. Phys.* **3**(3), 207–223 (2021).
39. Z. Huang and L. Cao, "Quantitative phase imaging based on holography: trends and new perspectives," *Light Sci. Appl.* **13**(1), 145 (2024).
40. M. Chen, L. Tian, and L. Waller, "3D differential phase contrast microscopy," *Biomed. Opt. Express* **7**(10), 3940–3950 (2016).
41. N. G. Crawford et al., "Loci associated with skin pigmentation identified in African populations," *Science* **358**(6365), eaan8433 (2017).
42. O. C. Marina, C. K. Sanders, and J. R. Mourant, "Correlating light scattering with internal cellular structures," *Biomed. Opt. Express* **3**, 296–312 (2012).
43. G. Mie, "Beiträge zur Optik trüber Medien, speziell kolloidaler Metallösungen," *Ann. Phys., Lpz.* **330**(3), 377–445 (1908).
44. S. H. Gage, "Modern dark-field microscopy and the history of its development," *Trans. Am. Microsc. Soc.* **39**(2), 95–141 (1920).
45. X. Chen et al., "Nanometer precise red blood cell sizing using a cost-effective quantitative dark field imaging system," *Biomed. Opt. Express* **11**(10), 5950–5966 (2020).
46. X.-Y. Wan et al., "Real-time light scattering tracking of gold nanoparticles- bioconjugated respiratory syncytial virus infecting HEp-2 cells," *Sci. Rep.* **4**(1), 4529 (2014).
47. L. Veith et al., "Distribution of paramagnetic Fe_2O_3/SiO_2–core/shell nanoparticles in the rat lung studied by time-of-flight secondary ion mass spectrometry: no indication for rapid lipid adsorption," *Nanomaterials* **8**(8), 571 (2018).
48. A. I. Abdel-Fattah, M. S. El-Genk, and P. W. Reimus, "On visualization of sub-micron particles with dark-field light microscopy," *J. Colloid Interface Sci.* **246**(2), 410–412 (2002).
49. H. Lindner, G. Fritz, and O. Glatter, "Measurements on concentrated oil in water emulsions using static light scattering," *J. Colloid Interface Sci.* **242**(1), 239–246 (2001).
50. H. G. Merkus, *Particle Size Measurements: Fundamentals, Practice, Quality*, Springer, Dordrecht (2009).
51. V. Backman et al., "Measuring cellular structure at submicrometer scale with light scattering spectroscopy," *IEEE J. Sel. Top. Quantum Electron.* **7**(6), 887–893 (2001).
52. T. E. Moustafa et al., "Fabrication and validation of an LED array microscope for multimodal, quantitative imaging," *HardwareX* **13**, e00399 (2023).
53. Z. Liu et al., "Real-time brightfield, darkfield, and phase contrast imaging in a light-emitting diode array microscope," *J. Biomed. Opt.* **19**(10), 106002 (2014).
54. L. Tian and L. Waller, "Quantitative differential phase contrast imaging in an LED array microscope," *Opt. Express* **23**(9), 11394–11403 (2015).
55. E. A. Smith et al., "Receptor tyrosine kinase inhibition leads to regression of acral melanoma by targeting the tumor microenvironment," *J. Exp. Clin. Cancer Res.* (2024).
56. J. C. Crocker and D. G. Grier, "Methods of digital video microscopy for colloidal studies," *J. Colloid Interface Sci.* **179**(1), 298–310 (1996).
57. J. C. Contreras-Naranjo and V. M. Ugaz, "A nanometre-scale resolution interference-based probe of interfacial phenomena between microscopic objects and surfaces," *Nat. Commun.* **4**(1), 1919 (2013).
58. W. Song et al., "Wavelength-dependent optical properties of melanosomes in retinal pigmented epithelium and their changes with melanin bleaching: a numerical study," *Biomed. Opt. Express* **8**(9), 3966–3980 (2017).
59. D. Huang et al., "Identifying fates of cancer cells exposed to mitotic inhibitors by quantitative phase imaging," *Analyst* **145**(1), 97–106 (2019).

60. T. J. Mitchison and E. D. Salmon, "Mitosis: a history of division," *Nat. Cell Biol.* **3**(1), E17–E21 (2001).
61. A. Nyga et al., "Dynamics of cell rounding during detachment," *iScience* **26**(5), 106696 (2023).
62. J. Moore and E. Cerasoli, "Particle light scattering methods and applications," in *Encyclopedia of Spectroscopy and Spectrometry (Second Edition)*, J. C. Lindon, Ed., pp. 2077–2088, Academic Press, Oxford (2010).
63. H. Wang et al., "Fourier ptychographic topography," *Opt. Express* **31**(7), 11007–11018 (2023).
64. R. Horstmeyer et al., "Diffraction tomography with Fourier ptychography," *Optica* **3**(8), 827–835 (2016).
65. E. R. Polanco et al., "Multiparametric quantitative phase imaging for real-time, single cell, drug screening in breast cancer," *Commun. Biol.* **5**, 794 (2022).
66. S. Pradeep and T. A. Zangle, "Quantitative phase velocimetry measures bulk intracellular transport of cell mass during the cell cycle," *Sci. Rep.* **12**(1), 6074 (2022).

Tarek Moustafa is a PhD candidate in the Department of Chemical Engineering at the University of Utah. In 2018, he received his BSc in energy and bioprocess engineering from Zewail City of Science and Technology in Egypt. In 2019 he joined the Zangle lab. His research focuses on the development and applications of label-free imaging techniques to study single-cell behavior in real time.

Rachel L. Belote is an assistant professor in the Department of Molecular Genetics at The Ohio State University. She earned a BS in biochemistry from Rutgers University in 2008 and a PhD in cellular biophysics from Rockefeller University in 2016, followed by postdoctoral training at the Huntsman Cancer Institute, University of Utah. Her research investigates how cellular heterogeneity contributes to functional diversification within cell types in organ health and disease.

Edward R. Polanco is currently a materials science engineer at Gentex Corporation developing new processes for fabricating organic semiconducting materials. He started his career at UCLA where he studied the relationship between the biophysical properties of cancer cells and metastatic potential. Afterward, he pursued a PhD at the University of Utah where he designed a high-throughput platform for studying the heterogeneous response of cancer cells to therapy using both cell lines and primary cells.

Robert L. Judson-Torres is an associate professor in the Department of Dermatology and a Huntsman Cancer Institute Investigator at the University of Utah. He received his PhD in 2012 in biomedical sciences from the University of California, San Francisco, and began an NIH Director's Early Independence Fellowship in 2014. His research focuses on integrating single-cell-omics to understand the mechanisms of skin cancer initiation and progression.

Thomas A. Zangle is an associate professor in the Department of Chemical Engineering at the University of Utah and a member of the Huntsman Cancer Institute. He received his MS in 2007 and PhD in 2010 in mechanical engineering from Stanford University before postdoctoral training in the Department of Pathology at UCLA. His research focuses on the application of quantitative imaging to study cell biology and measure cancer cell response to therapy.